Journal of Materials Chemistry A

ROYAL SOCIETY OF CHEMISTRY

PAPER

View Article Online
View Journal | View Issue

Cite this: J. Mater. Chem. A, 2024, 12, 16491

Co/Li_2S of chemical confinement decorated electrochemically stable Co(OH)F nanoarrays enabling dendrite-free flexible 3D Li anodes†

Liubin Song,[a] Yixuan Wang,[a] Huaming Qian,[b] Mengxin Bai,[b] Qinchuan Chen,[b] Minzhi Xiao,[a] Tingting Zhao,*[a] Zhongliang Xiao,[a] Jingjing Wang[bc] and Xifei Li *[bc]

Lithium (Li) metal is regarded as a promising anode for high-energy-density Li-ion batteries because of its high theoretical specific capacity and low potential. Unfortunately, the safety issues derived from Li dendrite formation have hindered their commercialization. Thus, fabricating a flexible, three-dimensional (3D) composite Li anode is an effective strategy to suppress Li dendrite growth. Lithiophilic nanoarrays are commonly constructed on a 3D skeleton to increase its surface area and lithiophilicity. However, the lithiophilic nanoarrays are unstable due to the conversion reaction during Li plating/stripping. Therefore, designing composite nanoarrays with an electrochemically stable inner core and a lithiophilic outer shell is conducive to providing a large surface area and promoting uniform Li deposition. Herein, CoS_2 shell–Co(OH)F core composite nanowire arrays were prepared on carbon cloth (CoS_2–Co(OH)F/CC) to fabricate a flexible 3D composite Li anode (Li@CoS_2–Co(OH)F/CC), in which the electrochemically stable Co(OH)F core ensures the stability of the nanoarray and the lithiophilic CoS_2 shell facilitates uniform Li adsorption. Moreover, the Co/Li_2S configuration derived from the lithiation of CoS_2 could promote homogeneous Li deposition, in which the lithiophilic Li_2S phase and electron-conductive Co phase jointly facilitate uniform Li nucleation and charge transfer. Consequently, the symmetric cells and full cells paired with a $LiFePO_4$ (LFP) cathode based on the flexible Li@CoS_2–Co(OH)F/CC anode presented superior cycling stability.

Received 31st March 2024
Accepted 27th May 2024

DOI: 10.1039/d4ta02143f

rsc.li/materials-a

1. Introduction

Lithium-ion (Li-ion) batteries have been widely utilized in energy storage systems. However, the commercial Li-ion batteries' energy density is approximately 250 Wh kg^{-1}, which poses a challenge to meet the emerging power battery system's demands.[1,2] The commercially available Li-ion batteries employ a graphite anode with a specific capacity of only 372 mA h g^{-1}, whereas the Li metal anode exhibits a significantly higher specific capacity of 3860 mA h g^{-1} at a low potential (−3.04 V *vs.* the standard hydrogen electrode).[3,4] Therefore, the utilization of Li metal anodes exhibits promising potential for enhancing the energy density of Li-ion batteries. Nevertheless, safety concerns arising from Li dendrite formation have seriously hindered the progress of Li-metal batteries.[5–7]

In addressing such intractable issues, many strategies have been developed, including electrolyte modification,[8,9] artificial solid–electrolyte interface construction,[10–12] separator modification[13–15] and 3D electrode fabrication.[16–18] According to the theory of "Sand's time," the charge accumulation on some spots causes the local current density to exceed the limiting current density, which induces uncontrollable Li dendrite growth.[19,20] Among the strategies, fabricating a 3D Li metal anode can provide a large space to lower local current density and accommodate Li deposition, thereby decreasing the probability of Li dendrite formation.[21–23] Therefore, this strategy has great application potential, whereas the commonly used 3D skeletons are mostly lithiophobic, such as Ni foam,[24] Cu foam,[25] carbon nanotubes,[26] and carbon cloth (CC).[17,27] Introducing lithiophilic nanoarrays, including nanospheres, nanowires, and nanorods, onto the surface of a 3D skeleton is often performed to provide a larger surface area and physical space as well as to improve their lithiophilicity.[28–30] However, most lithiophilic nanoarrays consist of metallic compounds, which undergo a conversion reaction with Li during initial deposition and subsequently collapse in structure. As a result, they are unable to effectively regulate the subsequent Li plating/stripping process.[31,32] Therefore, constructing composite nanoarrays with an electrochemically stable inner core and a lithiophilic outer shell on a 3D skeleton is conducive to providing a stable structure and promoting uniform Li deposition.[33]

[a]School of Chemistry and Chemical Engineering, Changsha University of Science and Technology, Changsha 410114, China. E-mail: zhaott_468@163.com

[b]Institute of Advanced Electrochemical Energy, School of Materials Science and Engineering, Xi'an University of Technology, Xi'an 710048, PR China. E-mail: xfli@xaut.edu.cn

[c]Guangdong Yuanneng Technologies Co Ltd, Foshan, Guangdong, 528223, China

† Electronic supplementary information (ESI) available. See DOI: https://doi.org/10.1039/d4ta02143f

Herein, composite shell–core CoS_2–Co(OH)F nanowire arrays were constructed on CC (denoted as CoS_2–Co(OH)F/CC) to fabricate a flexible 3D composite Li anode (denoted as Li@CoS_2–Co(OH)F/CC). The Co(OH)F core is electrochemically stable, which can maintain the structure of the nanoarray and the large space to decrease current density and accommodate Li deposition. The lithiophilic CoS_2 shell can facilitate Li adsorption, and it will be transferred into the Co/Li_2S configuration after lithiation, in which the lithiophilic Li_2S phase could regulate the oriented Li deposition and the electron-conductive Co phase could ensure efficient charge transfer, thereby synergistically promoting homogeneous Li nucleation and deposition. Consequently, the symmetric cells based on the flexible Li@CoS_2–Co(OH)F/CC anode achieved superior cycling stability with a low overpotential (13 mV) over 2500 h cycles. When assembled with a $LiFePO_4$ (LFP) cathode, the LFP//Li@CoS_2–Co(OH)F/CC full cell delivered outstanding cycling stability (1500 cycles at 1C).

2. Results and discussion

The CoS_2–Co(OH)F/CC sample was prepared by a hydrothermal method and vulcanization (Fig. 1a). The XRD results showed that the CoS_2–Co(OH)F/CC sample is composed of CoS_2 (PDF #89-1492) and Co(OH)F (PDF #50-0827, Fig. 1b). Co and S are detected in the XPS spectra, whereas F is absent (Fig. 1c). Furthermore, the Co 2p spectrum can be fitted into two spin orbit doublets (Co^{2+} and Co^{3+}) and two satellite peaks (Fig. 1d). Two peaks of 163.1 eV and 164.3 eV are shown in the S 2p spectrograph (Fig. 1e), matching S $2p_{3/2}$ and S $2p_{1/2}$, respectively.[34–36] The Co 2p and S 2p core-level spectra confirm the presence of CoS_2. Considering the detection depth of XPS analysis, it indicated that the CoS_2 phase is on the outer surface, and Co(OH)F is in the inner core. The abovementioned results confirm the successful preparation of the shell–core CoS_2–Co(OH)F composite on CC.

The SEM images of the CoS_2–Co(OH)F/CC sample showed that its surface is covered with flower-like clusters that are composed of uniform needle-like nanorods (Fig. 2a–c). For comparison, the inadequate concentration of 1.0 mmol $Co(NO_3)_2 \cdot 6H_2O$ leads to uneven growth of nanowires (Fig. S1a†), while excessive concentration of 2.4 mmol $Co(NO_3)_2 \cdot 6H_2O$ results in agglomeration and accumulation (Fig. S1b†). An appropriate concentration of 1.7 mmol $Co(NO_3)_2 \cdot 6H_2O$ leads to uniform and dense nanowire clusters on the surface

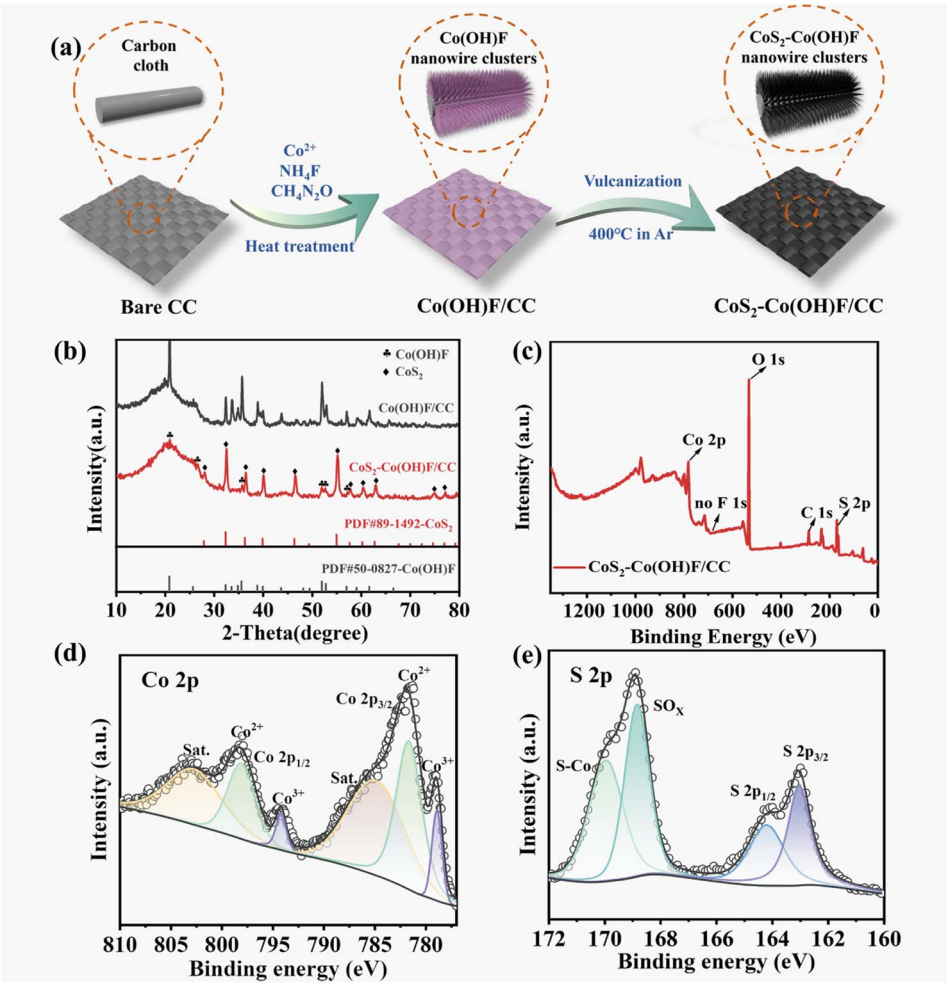

Fig. 1 (a) Schematic illustration showing the preparation of the CoS_2–Co(OH)F composite on the surface of CC. (b) XRD pattern and XPS spectra of the CoS_2–Co(OH)F: (c) full, (d) Co 2p and (e) S 2p spectra.

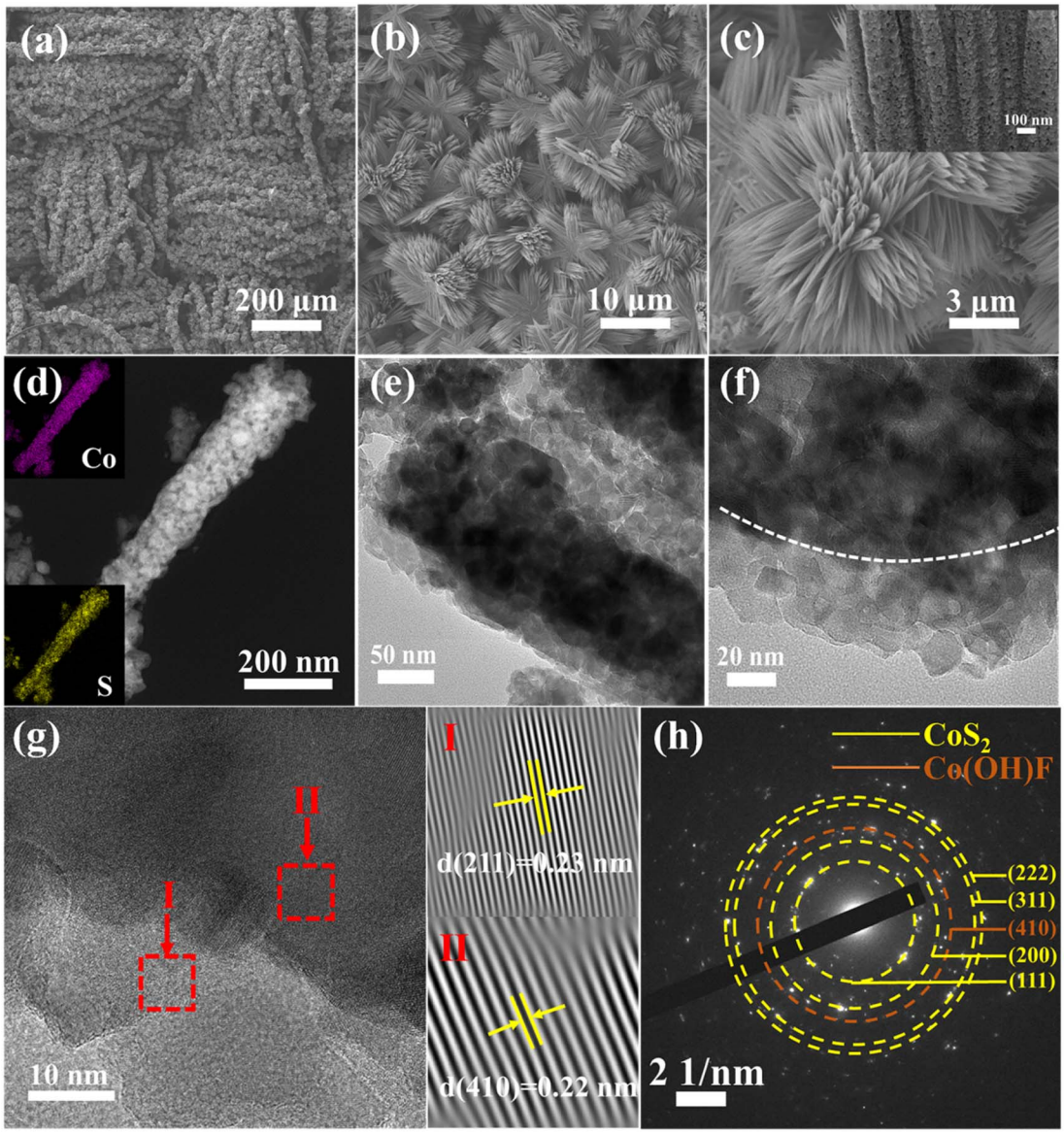

Fig. 2 (a–c) SEM images of CoS_2–Co(OH)F/CC nanowire clusters at different magnifications. (d) Elemental mapping, (e–g) TEM images, and (h) SAED pattern of the CoS_2–Co(OH)F nanorod.

of the CC with each carbon nanofiber encapsulated by the Co(OH)F clusters. In addition, the SEM images of the pure CC and Co(OH)F precursor clearly illustrate the intricate CC structure formed by interweaved carbon fibers and the nanowire cluster structure of the Co(OH)F precursor indicates that the vulcanization reaction does not alter the overall 3D framework (Fig. S2†). Moreover, the impact of the vulcanization degree on the morphology of the samples was analyzed by regulating the mass ratios of sublimed sulfur to the precursor at 1 : 1, 6 : 1, and 30 : 1. The XRD patterns demonstrate a gradual decrease in the peak intensity of the Co(OH)F core and an increase in the presence of the CoS_2 shell as the vulcanization degree increases (Fig. S3†), indicating a progressive variation in the Co(OH)F/CoS_2 core–shell structure. Furthermore, CoS_2–Co(OH)F/CC-6:1 displays a dense layer of CoS_2 nanoparticles, indicating the proper vulcanization of the sample. In contrast, CoS_2–Co(OH)F/CC (1 : 1) and CoS_2/CC (30 : 1) exhibit insufficient and excessive vulcanization, respectively, which demonstrates the exceptional characteristics of the CoS_2–CO(OH)F/CC-6 : 1 structure (Fig. S4†). The microstructure of the nanorods was further characterized by TEM and selected area electron diffraction (SAED) (Fig. 2d–h), which further confirms the presence of CoS_2 on the outer surface of the composite nanorod.[34,37] The elemental mapping of Co and S atoms indicated that the CoS_2 layer is distributed homogeneously on the surface (Fig. 2d). TEM characterization reveals obvious CoS_2 shell and Co(OH)F core structures, as shown in Fig. 2e and f. The lattice fringe in zone I (Fig. 2g) corresponds to the (211) plane of CoS_2, while that in zone II corresponds to the (410) plane of Co(OH)F, which further confirms the presence of a shell–core structure of CoS_2–Co(OH)F. The width of a single nanorod is approximately 157 nm and sufficient space exists between the nanorods, which

is conducive to providing a large surface area and promoting Li deposition.

To reveal the effect of the CoS_2–Co(OH)F nanorod on the surface lithiophilicity of CC, Li adsorption energy (E_a) was calculated by using the density functional theory (DFT). E_a values on the different sites of C are −1.01, −2.12, and −1.02 eV, whereas E_a values on the different sites of CoS_2 are −2.86, −2.68, and −2.68 eV, indicating a stronger interaction between CoS_2 and Li than that between C and Li (Fig. 3a–c and S5†). Therefore, the surface lithiophilicity of CC is remarkably improved after being modified by the CoS_2–Co(OH)F nanorod, which could facilitate initial Li adsorption or nucleation.

During the initial lithiation process, the discharge curve of the CoS_2–Co(OH)F/CC//Li half-cell presented an evident voltage plateau at approximately 1.5 V (Fig. S6†), which indicates the conversion reaction of CoS_2 into Li_2S and Co.[38] Moreover, the XPS analysis of the CoS_2–Co(OH)F/CC sample after the conversion reaction shows a peak at 162.2 eV in the XPS S 2p spectrum, a peak at 54.6 eV in the Li 1s spectrum, and a peak at 777.8 eV in the Co 2p spectrum, which indicates the presence of Li_2S and Co on the outer surface of the nanorod (Fig. 3d–f).[39,40] Furthermore, E_a values on Co and Li_2S are −2.69 and −4.28 eV, respectively, which indicates a stronger interaction between Li_2S and Li than that between Co and Li (Fig. 3g–i and S7†).[41] The charge density difference (Fig. 3j) between Co and Li_2S also showed that the charge distribution within Li_2S compared with that of Co is more favorable for Li adsorption. Therefore, Li_2S within the Co/Li_2S configuration could regulate the preferential Li deposition on the Li_2S and Co phases to promote a uniform Li deposition. The electron-conductive Co network is conducive to charge transfer.

To reveal the effect of Co/Li_2S configuration–derived chemical confinement on regulating Li nucleation and deposition, the SEM images of CoS_2–Co(OH)F/CC and pure CC after electrochemical deposition of different capacities of Li were observed. First, after discharging to 1 and 0.01 V, the CoS_2–Co(OH)F/CC sample maintains a flower-like structure composed of nanorods (Fig. S8†), which can be attributed to the electrochemically stable Co(OH)F core within the CoS_2–Co(OH)F shell–core structure. Additionally, the peak density in the XRD pattern assigned to the Co(OH)F core in the CoS_2/CC-30 : 1 sample diminished with increasing degree of vulcanization, showing vulnerable structure stability after lithiation (Fig. S9†) and further validating the stable shell–core structure of CoS_2–Co(OH)F/CC (6 : 1). After depositing Li with a capacity of 2 mA h cm^{-2}, the CoS_2–Co(OH)F/CC sample presented a flower-like structure with Li deposits

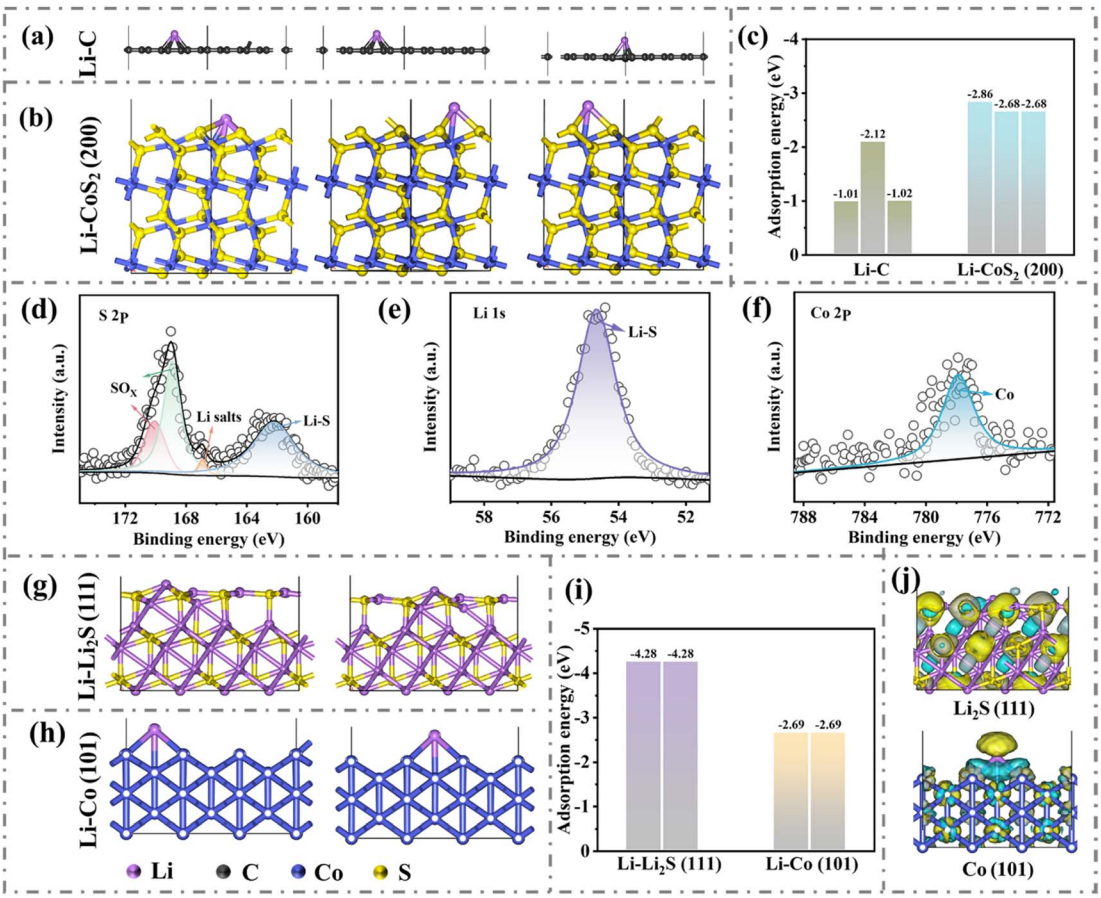

Fig. 3 Li adsorption geometry on the (a) C layer and (b) CoS_2 (200) plane, and (c) the corresponding E_a values. XPS analysis of CoS_2–Co(OH)F/CC after discharging to 0.01 V: (d) S 2p, (e) Li 1s and (f) Co 2p spectra. The Li adsorption geometry on (g) Li_2S (111) and (h) Co (101) planes, and (i) the corresponding E_a values. (j) Charge density differences of Li on the surfaces of Li_2S (111) and Co (101). The blue and yellow spheres represent electron accumulation and depletion, respectively.

surrounding the nanowire clusters and filling in the space between nanorods (Fig. S10†). With the increase in the capacity of deposited Li to 5, 8, and 11 mA h cm^{-2}, the Li metal gradually fills in the gaps between the flower-like structure and covers the surface homogenously (Fig. 4a). Conversely, disordered mossy Li was formed on the surface of CC because of its lithiophobic properties, leading to non-uniform Li deposition (Fig. 4b). Hence, the Co/Li_2S-modified Co(OH)F nanoarrays could not only accommodate Li and but also facilitate rapid charge transfer, thus promoting the Li plating process. The structure stability of the CoS_2–Co(OH)F/CC framework during Li plating/stripping is further explored. The SEM images of the CoS_2–Co(OH)F/CC framework after plating 5, 8 and 11 mA h cm^{-2} Li and stripping 5, 8 and 11 mA h cm^{-2} Li showed that the decorated-Co(OH)F nanoarray ensures reversible Li plating/stripping and maintains stable structure integrity (Fig. 4c). In contrast, mossy Li deposits still exist on the CC surface because of the formation of "dead Li" (Fig. 4d). After 50 cycles of Li plating/stripping (5 mA h cm^{-2}), the CoS_2–Co(OH)F/CC sample maintains a well-preserved flower-like structure, which greatly contributes to

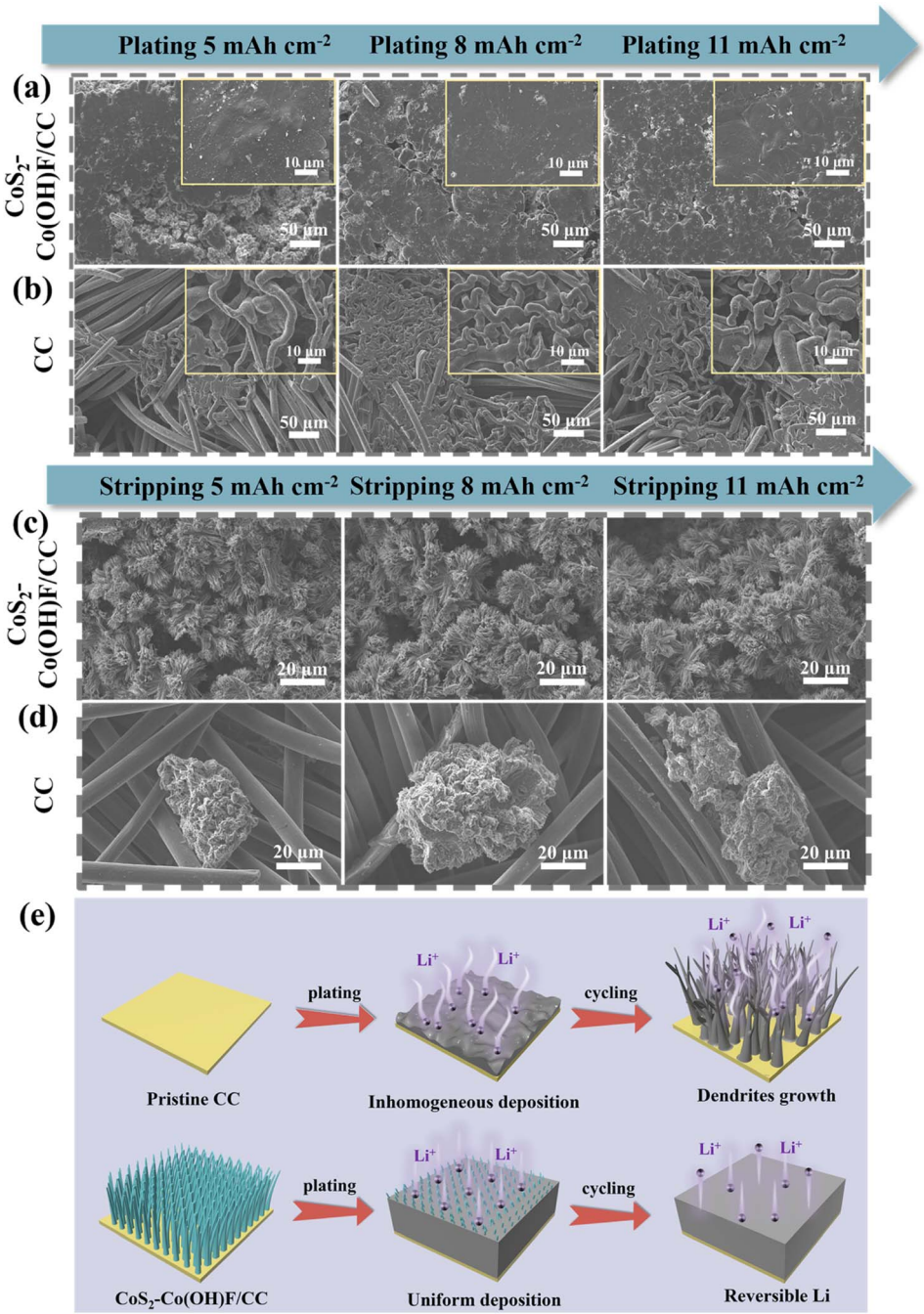

Fig. 4 SEM images of the (a) CoS_2–Co(OH)F/CC framework and (b) CC after plating different amounts of Li. SEM images of the (c) CoS_2–Co(OH)F/CC framework and (d) CC after Li stripping. (e) Schematic illustration showing the mechanism of the 3D CoS_2–Co(OH)F/CC skeleton in suppressing Li dendrite growth.

prolonged cycling stability (Fig. S11†). This finding indicated that the Co/Li_2S configuration-decorated electrochemically stable Co(OH)F nanoarray could effectively regulate the homogeneous Li deposition (Fig. 4e), in which the Co(OH)F nanoarray provides a "physical space" to accommodate Li and the Co/Li_2S-derived "chemical confinement" promotes Li adsorption and uniform Li distribution.[27,42]

To assess the electrochemical characteristics of the CoS_2–Co(OH)F/CC sample, coulombic efficiency (CE) and nucleation overpotential based on the half-cells were tested. As shown in Fig. 5a, at 0.5 mA cm^{-2} current density and 1 mA h cm^{-2} capacity, the CoS_2–Co(OH)F/CC//Li half-cell exhibits a consistent operational stability for 250 cycles with an average CE exceeding 99%. When increasing the current density and capacity to 1 mA cm^{-2} and 1 mA h cm^{-2}, 3 mA cm^{-2} and 1 mA h cm^{-2}, and 3 mA cm^{-2} and 3 mA h cm^{-2}, the CEs of half-cells remain over 99% (Fig. 5b and S12†). By contrast, the CEs of the CC//Li half-cell are markedly lower than that of CoS_2–Co(OH)F/CC, with inferior cycling stability. This impressive achievement can be credited to the Co/Li_2S-derived "chemical confinement" in facilitating Li plating and stripping as well as the stable Co(OH)F nanoarrays in ensuring structural stability. In addition, the overpotentials of the CoS_2–Co(OH)F/CC and CC samples at different current densities were investigated (Fig. 5c and S13†). The overpotentials of CoS_2–Co(OH)F/CC are lower than that of CC at all tested current densities (Fig. 5d), which can be attributed to the effect of the lithiophilic and electron-conductive Co/Li_2S configuration in promoting Li nucleation.

The assembled symmetric cells were utilized to explore the cycling stability and interface stability of the electrodes. The composite Li metal anode is obtained through the electrodeposition method. In contrast to the Li infusion method,[43] the electrodeposition method allows for precise control over the amount of deposited Li and ensures a uniform morphology, as shown in Fig. S14.† As shown in Fig. 5e, the Li@CoS_2–Co(OH)F/CC-based symmetric cells can operate stably for 2500 h with an overpotential of approximately 13 mV (1 mA cm^{-2}, 1 mA h cm^{-2}). In contrast, Li foil symmetric cells presented a large overpotential (25 mV) and poor cycle performance (500 h) under the same conditions. The Li@CC symmetric cells show even worse performance with overpotential increasing from 78.9 to 128 mV, indicating highly unstable Li plating/stripping behavior. During the initial cycle, the symmetric cells based on Li@CoS_2–Co(OH)F/CC exhibited a higher overpotential compared to symmetric cells based on Li foil, which illustrates the longer formation period of the SEI film on the surface of Li@CoS_2–Co(OH)F/CC than on that of Li. This is because pure Li metal is more active and prone to react with electrolyte and form the SEI film,[6] while the Co/Li_2S derived composite Li metal is more stable. Furthermore, the Li@CoS_2–Co(OH)F/CC symmetric cells still exhibited a prolonged cycle life of 1200 h and maintained an overpotential of 16 mV at 3 mA cm^{-2}/1 mA h cm^{-2} (Fig. 5f). However, the Li@CC and Li foil symmetric

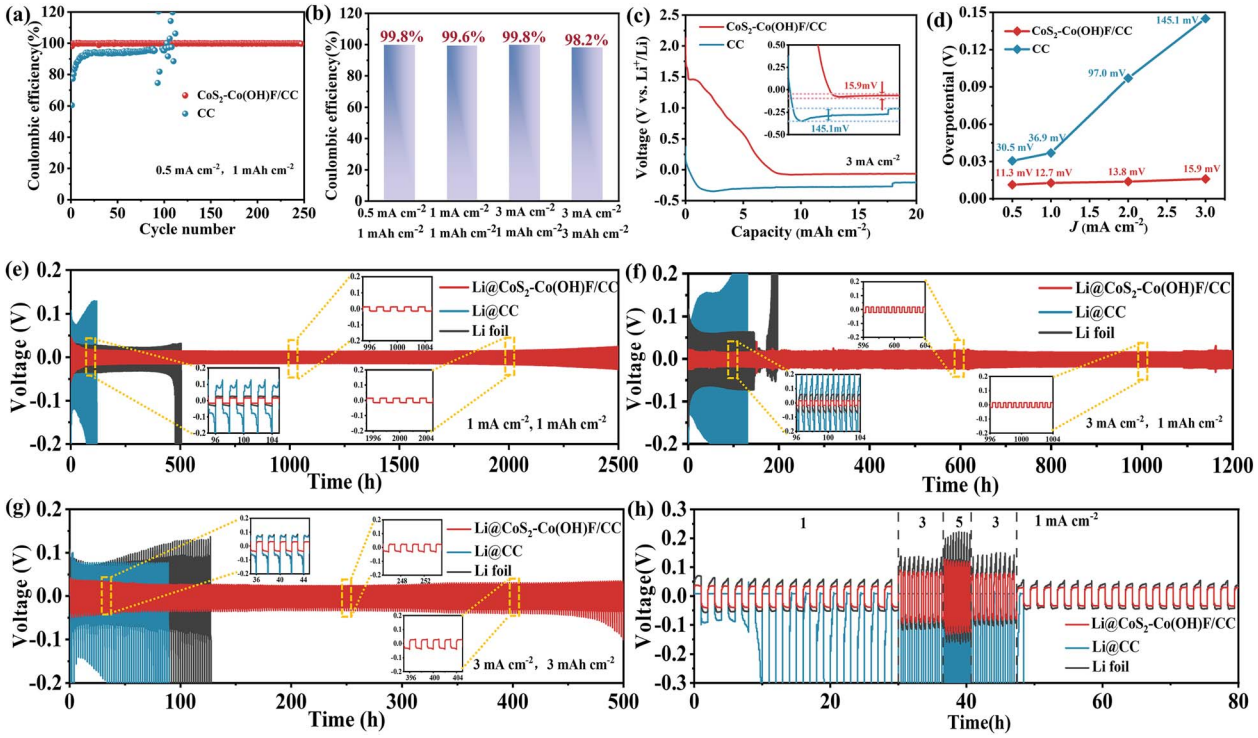

Fig. 5 (a) CE of CC//Li and CoS_2–Co(OH)F/CC//Li half cells at a current density of 0.5 mA cm^{-2} with a capacity of 1 mA h cm^{-2}. (b) The CE values of the half cells at different current densities and capacities. (c) Voltage profiles for Li nucleation on the CC and CoS_2–Co(OH)F/CC electrodes at 3 mA cm^{-2}. (d) Li nucleation overpotentials on CC and CoS_2–Co(OH)F/CC electrodes at different current densities. Cycling performance of Li foil, Li@CC and Li@CoS_2–Co(OH)F/CC-based symmetric cells at (e) 1 mA cm^{-2}/1 mA h cm^{-2}, (f) 3 mA cm^{-2}/1 mA h cm^{-2} and (g) 3 mA cm^{-2}/3 mA h cm^{-2}. (h) Rate capability of Li foil, Li@CC and Li@CoS_2–Co(OH)F symmetric cells.

cells showed voltage fluctuations after 105 and 166 h, respectively. Moreover, the Li@CoS_2–Co(OH)F/CC-based cell still exhibited satisfactory cycling stability with a small overpotential for 500 h when the capacity further increases to 3 mA cm^{-2}/3 mA h cm^{-2} (Fig. 5g). The rate capability of Li foil, Li/CC, and Li@CoS_2–Co(OH)F/CC-based symmetric cells was also investigated (Fig. 5h). The Li@CoS_2–Co(OH)F/CC-based symmetric cell presented exceptional reversibility with a lower overpotential compared with the other two symmetric cells.

To reveal the cause of the remarkable cycling performance and rate capability of the Li@CoS_2–Co(OH)F/CC-based cells, the Nyquist plot of the EIS spectra of Li foil, Li@CC, and Li@CoS_2–Co(OH)F/CC-based symmetric cells at the 5th and 100th cycles was captured (Fig. 6a and b). At the 5th cycle, the charge transfer resistance (R_{ct}) of Li foil, Li@CC, and Li@CoS_2–Co(OH)F/CC symmetric cells is 44.78 Ω, 31.4 Ω, and 26.1 Ω, respectively. At the 100th cycle, the R_{ct} of Li foil and Li@CoS_2–Co(OH)F/CC symmetric cells is 5.5 Ω and 1.1 Ω, respectively (the Li@CC symmetric cells failed before the 100th cycle). The smaller R_{ct} of the Li@CoS_2–Co(OH)F/CC-based cell indicated faster Li^+ transport and a more stable electrolyte/electrode interface. To reveal the relationship between microstructural stability and long-term cycling stability, the surface morphology of Li@CoS_2–Co(OH)F/CC and Li foil-based symmetric cells after the 20th, 50th, and 100th cycles was detected (Fig. 6c–h). The Li@CoS_2–Co(OH)F/CC electrode maintains a homogeneous and integral surface covered by Li metal (Fig. 6c–e). However, "dead Li" appeared on the surface of the Li foil even after 20 cycles, and severe cracks occurred after 100 cycles (Fig. 6f–h). Therefore, the Li@CoS_2–Co(OH)F/CC anode could maintain remarkable structure stability and effectively suppress Li dendrite formation during repeated Li plating/stripping.

To confirm the potential application of the Li@CoS_2–Co(OH)F/CC anode in full cells, the full cells with LFP as the cathode and Li foil and Li@CoS_2–Co(OH)F/CC as the anode were assembled (denoted as LFP//Li and LFP//Li@CoS_2–Co(OH)F/CC full cells). The discharge capacities of LFP//Li@CoS_2–Co(OH)F/CC full cells are 143.8, 135.5, 126.8, 117.4, 110.5 and 101.5 mA h g^{-1} at 0.2, 0.5, 1, 2, 3, and 5C, respectively (Fig. 7a), which are significantly higher than those of LFP//Li full cells. The charge–discharge profiles of LFP//Li@CoS_2–Co(OH)F/CC and LFP//Li full cells at different rates are shown in Fig. 7b and c. The LFP//Li@CoS_2–Co(OH)F/CC cell presented a more stable charge–discharge platform and lower voltage polarization than those of the LFP//Li cell. In addition, the cycling performance of the full cells was tested at 1C (Fig. 7d). The LFP//Li@CoS_2–Co(OH)F/CC cell demonstrated excellent cycling stability for 1500 cycles at 1C with a discharge capacity of

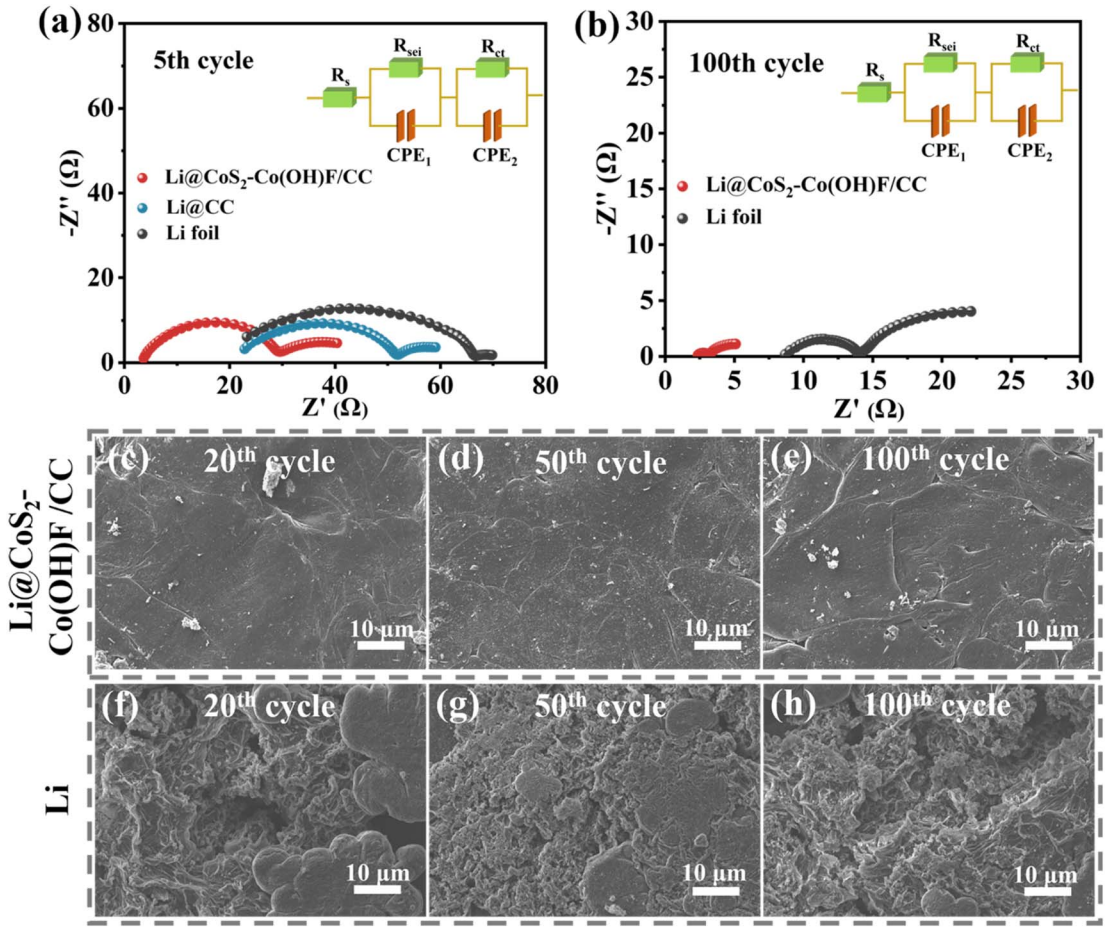

Fig. 6 (a and b) Nyquist plot of Li foil, Li@CC and Li@CoS_2–Co(OH)F/CC-based symmetric cells at different cycles. SEM images of (c–e) the Li@CoS_2–Co(OH)F/CC and (f–h) Li foil electrode after different cycles.

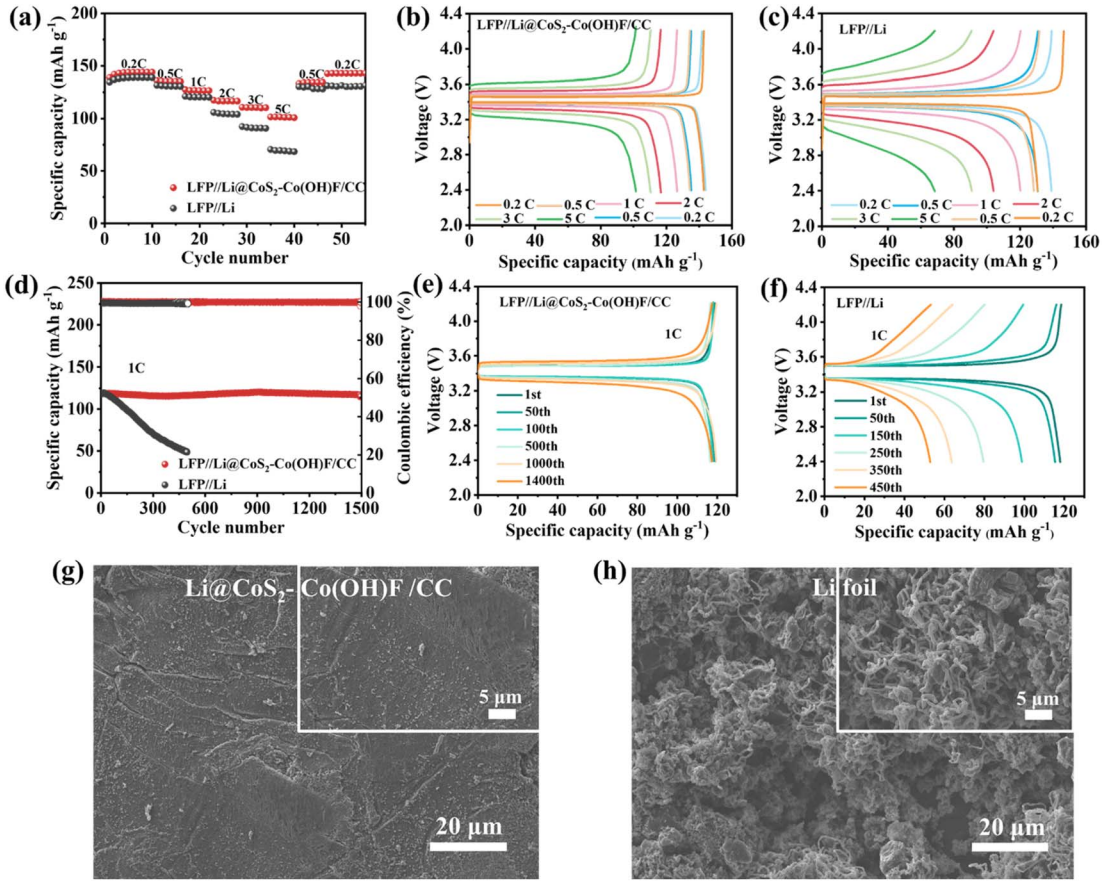

Fig. 7 (a) Rate capability and (b and c) charge–discharge profiles of LFP//Li@Li@CoS_2–Co(OH)F/CC and LFP//Li full cells at various rates ranging from 0.2C to 5C. (d) Cycle performance and (e and f) charge–discharge profiles of LFP//Li@CoS_2–Co(OH)F/CC and LFP//Li full cells at 1C. The SEM images of the corresponding anode for (g) LFP//Li@CoS_2–Co(OH)F/CC and (h) LFP//Li full cells after 200 cycles at 1C.

119.3 mA h g^{-1} compared with the LFP//Li full cell. Meanwhile, the Li@CoS_2–Co(OH)F/CC cell exhibited a more stable charge–discharge platform and lower voltage polarization than the LFP//Li full cell at different cycles (Fig. 7e). However, the discharge capacity of the LFP//Li full cell gradually decreased from the initial cycle because of the presence of Li dendrites. Moreover, the surface morphology of the anode in LFP//Li@CoS_2–Co(OH)F/CC and LFP//Li full cells was observed by SEM. As shown in Fig. 7g and S15a, b,† the Li@CoS_2–Co(OH)F/CC electrode still maintains a flat and uniform Li coating without any unwanted separation or smashing after 200 and 300 cycles. By contrast, unfavorable phenomena such as volume cracks and Li dendrites are observed in the Li foil of LFP//Li full cells (Fig. 7h and S15c, d†). The good cycling stability and rate performance of Li@CoS_2–Co(OH)F/CC-based symmetric cells and full cells are attributed to the Li_2S/Co configuration-decorated Co(OH)F nanoarray in stabilizing Li plating and stripping.

3. Conclusion

A highly stable lithiophilic and electron-conductive CoS_2–Co(OH)F shell–core nanoarray was successfully prepared on the CC skeleton to fabricate a flexible 3D Li metal anode. The electrochemically stable Co(OH)F core within the nanoarrays ensures structural stability during repeated Li plating/stripping, thereby accommodating Li deposition *via* the large area space between the nanoarrays. Meanwhile, the Co/Li_2S configuration formed on the outer surface of the nanoarrays could not only regulate the preferential Li plating on lithiophilic Li_2S sites and then Co sites but also ensure the rapid charge transfer. This derived chemical confinement synergistically promotes further homogeneous Li plating. Based on these advantages, the as-prepared Li@CoS_2–Co(OH)F/CC-based symmetric cells presented exceptional cycling stability with a prolonged lifespan of 2500 h and an overpotential of only 13 mV. Furthermore, the LFP//Li@CoS_2–Co(OH)F/CC full cells exhibited a stable cycling stability for 1500 cycles at 1C and superior rate capability. Therefore, the flexible 3D Li@CoS_2–Co(OH)F/CC anode could stabilize the Li plating/stripping *via* the functional Co/Li_2S configuration-modified Co(OH)F nanoarrays.

4. Experimental section

4.1 Experimental materials

Cobalt nitrate hexahydrate ($Co(NO_3)_2 \cdot 6H_2O$), urea (CH_4N_2O) and ammonium fluoride (NH_4F) were acquired from Sinopharm Chemical Reagent Co., Ltd. Sublimed sulfur (S) purchased from Tianjin Yongsheng Fine Chemical Co., Ltd. The mentioned reagents are of analytical quality and can be used

without further purification. CC with a thickness of 360 μm was purchased from CeTech Co., Ltd.

4.2 Preparation of the flexible Li@CoS_2–Co(OH)F/CC anode

4.2.1 Surface treatment of the CC substrate. To enhance the hydrophilicity of CC, it underwent an initial ultrasonic cleaning process using deionized water and anhydrous ethanol for a duration of 30 minutes to eliminate any surface impurities. Subsequently, it was fully immersed in a solution consisting of diluted nitric acid and sulfuric acid at room temperature for a period of 24 hours. Following this, multiple rinses were performed with deionized water and anhydrous ethanol before being subjected to drying at a temperature of 80 °C for 12 h.

4.2.2 Preparation of the Co(OH)F nanoarrays on CC. The hydrothermal method was used to synthesize the Co(OH)F array on CC. The procedure involved dissolving 1.7 mmol of $Co(NO_3)_2 \cdot 6H_2O$, 20 mmol of NH_4F, and 20 mmol of CH_4N_2O in 40 mL of deionized water. The resulting mixture was stirred at room temperature for 2 h until a homogeneous pink solution was obtained. Then a pre-treated CC (3 cm × 3 cm) was added to the pink solution and transferred into a 50 mL polytetrafluoroethylene autoclave. The autoclave was placed in a 120 °C blast oven for 5 h. At the end of the reaction, the CC sample was repeatedly rinsed with deionized water and anhydrous ethanol. After drying, the Co(OH)F/CC sample was ultimately obtained.

4.2.3 Preparation of the shell–core CoS_2–Co(OH)F nanoarrays on CC. The shell–core CoS_2–Co(OH)F nanoarrays was prepared by a partial vulcanization reaction of the Co(OH)F array. The sublimed sulfur and Co(OH)F/CC precursor were placed in a tube furnace at a mass ratio of 6 : 1, with the sublimed sulfur upstream and the Co(OH)F/CC sample downstream. After annealing in an Ar environment at 400 °C for 1 h with a ramp rate of 5 °C min^{-1} and cooling down, the CoS_2–Co(OH)F/CC sample was obtained.

4.2.4 Preparation of the flexible Li@CoS_2–Co(OH)F@CC anode. The Li@CoS_2–Co(OH)F/CC composite anodes were fabricated by electrodepositing 10 mA h cm^{-2} of Li metal onto the CoS_2–Co(OH)F/CC sample at 1 mA cm^{-2} current density.

4.3 Material characterization

The materials were subjected to X-ray diffraction (XRD) analysis using a Bruker D8 Advance instrument, with Cu-Kα radiation (λ = 0.15418 nm) at 40 kV and 40 mA. X-ray photoelectron spectroscopy (XPS) was performed on an Escalab 250xi device manufactured by Thermo Fisher Scientific. Scanning electron microscopy (SEM) examination was conducted using a GeminiSEM 500 instrument. Transmission electron microscopy (TEM) images were captured utilizing a JEM 2100 PLUS microscope. To acquire the XPS data of Li_2S and Co after the lithiation of CoS_2, the battery was disassembled within a glove box filled with Ar gas (with O_2 levels below 0.1 ppm and H_2O levels below 0.1 ppm). The target electrode was rinsed with glycol dimethyl ether and dried in the glove box. Then the electrode was transferred to the cavity of the XPS instrument using a transfer bunker under vacuum to prevent oxidation.[44]

4.4 Electrochemical measurements

The electrochemical performance was evaluated by conducting tests on CR2032 coin cells that were assembled in the glove box. In the half-cell configuration, a working electrode of the CoS_2–Co(OH)F@CC sample with a 12 mm diameter was employed, while a counter electrode consisting of Li foil with a 14 mm diameter was utilized. Celgard 2300 was used as the separator and 1.0 M LiTFSI dissolved in 1,3-dioxolane/1,2-dimethoxyethane (DOL/DME, 1 : 1, v/v) with 2 wt% $LiNO_3$ was used as the electrolyte. The electrolyte volume in each cell was regulated to 60 μL. When testing the CE, the cell was charged to 1 V at a small current of 0.1 mA cm^{-2} and cycled 5 cycles to form a stable solid electrolyte interface. The electrochemical impedance spectroscopy (EIS) test was conducted using an electrochemical workstation within the frequency range of 100 kHz to 10 mHz. The full cells were constructed using the Li@CoS_2–Co(OH)F/CC anode and $LiFePO_4$ (LFP) cathode with an active mass loading of ~2 mg cm^{-2}. LFP powder, Super P and polyvinylidene fluoride (8 : 1 : 1 wt%) were dissolved in *N*-methylpyrrolidone (NMP) solvent, and the LFP cathode was prepared by a blade-casting method on Cu foil. The concentration of the electrolyte used was 1 M $LiPF_6$ in EC/DEC (1 : 1, v/v), with a controlled dosage of 80 μL for each cell. The voltage range for the full cells was maintained at 2.4~4.2 V. The galvanostatic charge–discharge tests were conducted using a Neware battery test system (CT-4008T, Shenzhen, China).

4.5 Theoretical calculations

The GGA-PBE functional was utilized to depict the electron exchange and correlation.[45–47] The wave functions were expanded using the DNP-4.4 file, which represents a localized basis set incorporating a polarization d-function.[48,49] The spin unrestricted was used in all the calculations because the four models are open-shell systems.[47,50] The effective core potentials (ECP) were employed to treat the core electrons of the metal atoms,[51–53] while a uniform orbital cutoff of 5.0 Å was applied for all atoms. For the purpose of geometry optimization, the thresholds for achieving convergence were defined as 2×10^{-5} Ha for energy, 4×10^{-3} Ha $Å^{-1}$ for maximum force, and 5×10^{-3} Å for maximum displacement. Additionally, a SCF convergence criterion of 1.0×10^{-5} Ha was set to ensure accurate determination of electronic energy. The calculation of adsorption energy (E_{ads}) is performed using the equations provided below:[46]

$$E_{ads} = (E_{total} - E_{sub} - E_{Li})$$

where E_{total}, E_{sub} and E_{Li} represent the total energy of Li adsorption and non-adsorbed systems, and the energy of Li atoms in the metallic phase structure, respectively.

Author contributions

Liubin Song: investigation, methodology, writing – review & editing. Yixuan Wang: investigation, methodology, data curation, writing – original draft. Huaming Qian: data curation, investigation, writing – original draft, writing – review & editing.

Mengxin Bai: data curation, methodology, visualization, writing – review & editing. Qinchuan Chen: data curation, validation, writing – review & editing. Minzhi Xiao: data curation, methodology, writing – review & editing. Zhongliang Xiao: writing – original draft, writing – review & editing. Tingting Zhao: visualization, writing – original draft, writing – review & editing. Jingjing Wang: validation, writing – original draft, writing – review & editing. Xifei Li: conceptualization, formal analysis, funding acquisition, project administration, resources, supervision, writing – original draft, writing – review & editing.

Conflicts of interest

The authors declare that they have no known competing financial interests or personal relationships that could have appeared to influence the work reported in this paper.

Acknowledgements

This work was financially supported by the National Natural Science Foundation of China (21501015), Hunan Provincial Natural Science Foundation of China (2022JJ30604), Hunan Provincial Key Laboratory of Materials Protection for Electric Power and Transportation (2022CL01) and Foshan Science and Technology Innovation Team Project (1920001004098).

References

1 J. Wang, L. Wang, H. Xu, L. Sheng and X. He, *Green Energy Environ.*, 2024, **9**, 454–472.
2 J.-F. Ding, Y.-T. Zhang, R. Xu, R. Zhang, Y. Xiao, S. Zhang, C.-X. Bi, C. Tang, R. Xiang, H. S. Park, Q. Zhang and J.-Q. Huang, *Green Energy Environ.*, 2023, **8**, 1509–1530.
3 L. Wang, P. Gao, C. Li and H. Li, *Nano Res.*, 2023, **16**, 8053–8054.
4 M. Zhu, X. Zhao, R. Yan and J. Zhang, *Curr. Opin. Solid State Mater. Sci.*, 2023, **27**, 101079.
5 S. Qian, H. Chen, M. Zheng, Y. Zhu, C. Xing, Y. Tian, P. Yang, Z. Wu and S. Zhang, *Energy Storage Mater.*, 2023, **57**, 229–248.
6 W. Tang, J. Ma, X. Zhang, Y. Li, S. Meng, Y. Zhang, H. Dong, R. Liu, R. Gao and M. Feng, *Energy Storage Mater.*, 2024, **64**, 103084.
7 H. Yuan, X. Ding, T. Liu, J. Nai, Y. Wang, Y. Liu, C. Liu and X. Tao, *Mater. Today*, 2022, **53**, 173–196.
8 O. B. Chae and B. L. Lucht, *Adv. Energy Mater.*, 2023, **13**, 2203791.
9 H. Chen, Y.-X. Xie, S.-S. Liu, H. Peng, W.-C. Zheng, P. Dai, Y.-X. Huang, M. Sun, M. Lin, L. Huang and S.-G. Sun, *ACS Appl. Mater. Interfaces*, 2023, **15**, 45834–45843.
10 C. Zhang, Y. Yang, Y. Sun, L. Duan, Z. Mei, Q. An, Q. Jing, G. Zhao and H. Guo, *Sci. China Mater.*, 2023, **66**, 2591–2600.
11 X. Ding, Y. Xin, Y. Wang, M. Wang, T. Song and H. Gao, *ACS Sustain. Chem. Eng.*, 2023, **11**, 6879–6889.
12 C. Liu, Z. Yuan, K. Chen, Y. Jiang, M. Yue, K. Dong, Y. Liu, Y. Guo and Y. Wang, *ACS Appl. Mater. Interfaces*, 2023, **15**, 56356–56364.
13 C. Wang, Z. Hao, Y. Hu, Y. Wu, J. Liu, Y. Jin, H. Wang and Q. Zhang, *J. Mater. Chem. A*, 2023, **11**, 8131–8140.
14 C. Zu, J. Li, B. Cai, J. Qiu, Y. Zhao, Q. Yang, H. Li and H. Yu, *J. Power Sources*, 2023, **555**, 232336.
15 T. Naren, R. Jiang, P. Qing, S. Huang, C. Ling, J. Lin, W. Wei, X. Ji, Y. Chen, Q. Zhang, G.-C. Kuang and L. Chen, *ACS Nano*, 2023, **17**, 20315–20324.
16 X. Cui, J. Yang, Z. Xu, Q. Liu, Y. Nuli and J. Wang, *Nano Energy*, 2022, **95**, 107013.
17 F. Cheng, X. Yang, O. Ka, L. Wen, X. Wang and W. Lu, *J. Mater. Chem. A*, 2023, **11**, 4205–4219.
18 C. Wei, Z. Yao, J. Ruan, Z. Song, A. Zhou, Y. Song, D. Wang, J. Jiang, X. Wang and J. Li, *Chin. Chem. Lett.*, 2024, **35**, 109330.
19 S. Xia, C. Yang, Z. Jiang, W. Fan, T. Yuan, Y. Pang, H. Sun, T. Chen, X. Li and S. Zheng, *Adv. Compos. Hybrid Mater.*, 2023, **6**, 198.
20 W. Zhang, J. Wang, H. Zhang, Q. Dong, S. Zhang, B. Sun, Z. Chen, H. Guo, X. Han, Y. Deng and W. Hu, *Small Struct.*, 2024, **5**, 2300358.
21 X. He, K. Zhang, Z. Zhu, Z. Tong and X. Liang, *Chem. Soc. Rev.*, 2024, **53**, 9–24.
22 H. Liang, L. Wang, L. Sheng, H. Xu, Y. Song and X. He, *Electrochem. Energy Rev.*, 2022, **5**, 23.
23 Y. Fang, S. L. Zhang, Z. P. Wu, D. Luan and X. W. D. Lou, *Sci. Adv.*, 2021, **7**, eabg3626.
24 K. Tang, J. Xiao, M. Long, J. Chen, H. Gao and H. Liu, *Sustainable Mater. Technol.*, 2022, **32**, e00408.
25 M. Sun, K. Huang, X. Lv, G. Ai, F. Gao, C. Lai, T. Zhang and W. Mao, *ACS Appl. Mater. Interfaces*, 2023, **15**, 38956–38964.
26 Y. Yang, E. Hu, Y. Zhu, W. Cao, J. Zhang, Z. Mao, X. Gao and Z. Chen, *Chem. Eng. J.*, 2023, **477**, 146879.
27 H. Qian, X. Li, Q. Chen, W. Liu, Z. Zhao, Z. Ma, Y. Cao, J. Wang, W. Li, K. Xu, K. Zhang, W. Yan, J. Zhang and X. Li, *Adv. Funct. Mater.*, 2023, **34**, 2310143.
28 S. Zhang, S. Xiao, D. Li, J. Liao, F. Ji, H. Liu and L. Ci, *Energy Storage Mater.*, 2022, **48**, 172–190.
29 H. Wang, Y. Liu, Y. Li and Y. Cui, *Electrochem. Energy Rev.*, 2019, **2**, 509–517.
30 Y. Fang, Y. Zeng, Q. Jin, X. F. Lu, D. Luan, X. Zhang and X. W. Lou, *Angew. Chem., Int. Ed.*, 2021, **60**, 8515–8520.
31 X. Liu, K. Long, P. Qing, S. Huang, P. Xiao, C. Ling, Z. Wu and L. Chen, *Sci. China Mater.*, 2023, **66**, 4349–4356.
32 G.-D. Yang, B. Li, Y.-H. Song, L. Ding, S.-G. Gong, X.-L. Wu, J.-P. Zhang, Y.-F. Li and H.-Z. Sun, *Electrochim. Acta*, 2022, **430**, 141035.
33 Q. Wang, T. Lu, Y. Xiao, J. Wu, L. Guan, L. Hou, H. Du, H. Wei, X. Liu, C. Yang, Y. Wei, H. Zhou and Y. Yu, *Electrochem. Energy Rev.*, 2023, **6**, 22.
34 X. Wang, X. Zhong, Z. Zha, G. He, Z. Miao, H. Lei, Q. Luo, R. Zhang, Z. Liu and L. Cheng, *Appl. Mater. Today*, 2020, **18**, 100464.
35 Q. Li, Y. Zhao, H. Liu, P. Xu, L. Yang, K. Pei, Q. Zeng, Y. Feng, P. Wang and R. Che, *ACS Nano*, 2019, **13**, 11921–11934.
36 G. Cao, X. Li, R. Duan, K. Xu, K. Zhang, L. Chen, Q. Jiang, J. Li, J. Wang, M. Li, N. Wang, J. Wang, Y. Xi, C. Xie and W. Li, *Nano Energy*, 2023, **116**, 108755.

37 C. Guan, X. Liu, A. M. Elshahawy, H. Zhang, H. Wu, S. J. Pennycook and J. Wang, *Nanoscale Horiz.*, 2017, **2**, 342–348.
38 T. Zhang, M. Wu, H. Gu, H. Yu, M. Zhou, X. Guo, Y. Liu, X. Zheng, Q. Kong and J. Zhang, *J. Energy Storage*, 2023, **73**, 108981.
39 R. Zhang, B. Chen, C. Shi, J. Sha, L. Ma, E. Liu and N. Zhao, *Small*, 2023, **19**, 2208095.
40 G. Cao, X. Li, L. Chen, R. Duan, J. Li, Q. Jiang, J. Wang, M. Li, M. Li, J. Wang, Y. Xi, W. Li and J. Peng, *Small*, 2024, 2311174.
41 J. Pan, J. Li, H. Dong, Y. Fang, K. Shi and Q. Liu, *Chem. Eng. J.*, 2022, **447**, 137401.
42 S. Ye, X. Chen, R. Zhang, Y. Jiang, F. Huang, H. Huang, Y. Yao, S. Jiao, X. Chen, Q. Zhang and Y. Yu, *Nano-Micro Lett.*, 2022, **14**, 187.
43 J. Cao, G. Qian, X. Lu and X. Lu, *Small*, 2023, **19**, 2205653.
44 F. She, A. Gao, P. Jiang, Y. Zhou, X. Zhang, M. Yang, L. Gong, J. Chen, X. Lu and F. Xie, *Vacuum*, 2023, **211**, 111893.
45 J. L. Vincent and P. A. Crozier, *Nat. Commun.*, 2021, **12**, 5789.
46 H. Wang, M. S. Bootharaju, J. H. Kim, Y. Wang, K. Wang, M. Zhao, R. Zhang, J. Xu, T. Hyeon, X. Wang, S. Song and H. Zhang, *J. Am. Chem. Soc.*, 2023, **145**, 2264–2270.
47 F. Fan, Z. Chen, A. Zhou, Z. Yang, Y. Zhang, X. He, J. Kang and W. Zhou, *Fuel*, 2023, **333**, 126351.
48 J. Wang, D.-g. Cheng, F. Chen and X. Zhan, *ACS Catal.*, 2022, **12**, 4501–4516.
49 C. Tang, G. Chen, Y. Liu, J. Wang, X. He, C. Xie, Z. He and J. Huang, *J. Mater. Chem. A*, 2023, **11**, 16671–16682.
50 D. Sun, Y. Chen, X. Yu, Y. Yin and G. Tian, *Chem. Eng. J.*, 2023, **462**, 142084.
51 Y. Pan, Y. Chen, K. Wu, Z. Chen, S. Liu, X. Cao, W.-C. Cheong, T. Meng, J. Luo, L. Zheng, C. Liu, D. Wang, Q. Peng, J. Li and C. Chen, *Nat. Commun.*, 2019, **10**, 4290.
52 C. Liao, J. M. Kasper, A. J. Jenkins, P. Yang, E. R. Batista, M. J. Frisch and X. Li, *JACS Au*, 2023, **3**, 358–367.
53 Y. Xie, J. Wu, G. Jing, H. Zhang, S. Zeng, X. Tian, X. Zou, J. Wen, H. Su, C.-J. Zhong and P. Cui, *Appl. Catal., B*, 2018, **239**, 665–676.